# Dalton Transactions

Accepted Manuscript






ROYAL SOCIETY OF CHEMISTRY

www.rsc.org/dalton

Journal Name

RSCPublishing

ARTICLE

# Synthesis, structure and properties of 2D lanthanide coordination polymers based on *N*-heterocyclic arylpolycarboxylate ligands

Cite this: DOI: 10.1039/xoxxoooooox

Received ooth January 2012,
Accepted ooth January 2012

DOI: 10.1039/xoxxoooooox

www.rsc.org/

**Li-Xin You,[a] Shu-Ju Wang,[a, c] Gang Xiong,[a] Fu Ding,[a] Katrien W. Meert,[b] Dirk Poelman,[b] Philippe F. Smet,[b] Bao-Yi Ren,[a] Yan-Wen Tian,[c] and Ya-Guang Sun*[, a]**

The reaction of 3-(2,4-dicarboxyphenyl)-2,6-pyridinedicarboxylic acid ($H_4$dppd) with rare earth nitrates under hydrothermal conditions generated a series of new two-dimensional (2D) coordination polymers, namely {$[La(Hdppd)(H_2O)_2\cdot(H_2O)_2]_n$(**1**), $[Ln_2(Hdppd)_2(H_2O)_4\cdot(H_2O)_3]_n$ [Ln = Sm(**2**), Eu(**3**)] and $[Ln(Hdppd)(H_2O)_3\cdot H_2O]_n$ [Ln = Gd(**4**), Tb(**5**), Dy(**6**), Ho(**7**), Er(**8**)] [Hdppd = 3-(2,4-dicarboxyphenyl)-2,6-pyridinedicarboxylic trivalent anion]}. The complexes were characterized by X-ray single-crystal diffraction, infrared spectroscopy, elemental analysis and thermogravimetric analysis. Luminescence spectroscopy of **3** and **5** showed bright red and green luminescence due to the $4f^n$-$4f^n$ transitions in $Eu^{3+}$ and $Tb^{3+}$ respectively, although the luminescence lifetime is shortened by non-radiative decay due to the presence of coordinating water molecules. The magnetic properties of **2**-**8** were measured and discussed. Compound **6** exhibits frequency dependent out-of-phase signals and ferromagnetic coupling exists in **8**.

## Introduction

The rational design and synthesis of coordination polymers is attracting increasing interest from chemistry researchers owing to their impressive structural diversity and many potential applications in various fields, such as luminescence [1], catalysis [2], magnetism [3], gas storage [4] and separation. [5] However, the final structures of coordination polymers are hardly controlled because the synthesis processes are influenced by many factors, such as the structural characteristics of the ligands, the coordination nature of lanthanides, the solvent preference, the pH value of the solution, the reaction temperature and the metal/ligand ratios. [6] Lanthanides are nevertheless of interest in constructing coordination polymers because most trivalent lanthanide ions can show exceptional magnetic properties and characteristic luminescent emissions in the visible to near-infrared part of the optical spectrum, arising from the $4f^n$ electronic configuration, and electronic transitions within this configuration. So far, many lanthanide coordination polymers (LCPs) have been prepared and their use in practical applications has been widely investigated [7]. However, a practical method for synthesizing LCPs with predictable and controlled geometries still remains challenging, due to the high and variable coordination numbers and flexible coordination environments of the lanthanide ions. [8] In addition, the ionic radius of the lanthanide ions decreases with increasing atomic number, which is often referred to as the lanthanide contraction. This may also affect the coordination number, resulting in different crystal structures [9].

Therefore, the appropriate choice of well-designed organic ligands is a useful approach for the synthesis of LCPs with potentially interesting properties. Among various ligands, the rigid aromatic ring-based polycarboxylic acid ligands have been successfully employed and documented in the preparation of various LCPs. It is well-known that arylpolycarboxylate ligands, such as biphenyl polycarboxylate [10] and *N*-heterocyclic arylpolycarboxylate ligands [11], play an important role in constructing novel LCPs with diverse structures and excellent properties. For example, UMCM-150, a highly porous crystalline material, was synthesized using the biphenyl-3,4',5-tricarboxylate ligand, and showed a high excess of gravimetric and volumetric $H_2$ uptake. [10f] In our recent work, Ni–Ln and Co–Ln series of 3D heterometallic–organic frameworks were constructed using 1*H*-benzimidazole-5,6-dicarboxylic acid ligands, which exhibit excellent photoluminescent and magnetic properties. [11e,11f] *N*-heterocyclic arylpolycarboxylate ligands usually adopt diverse coordination modes with metal ions due to their rich N and O donor atoms. In addition, they provide the possibility of hydrogen bonds for contributing to higher-dimensional structures. As an arylpolycarboxylate derivative, 3-(2,4-dicarboxyphenyl)-2,6-pyridinedicarboxylic acid ($H_4$dppd) possesses a pyridine ring and four carboxylate groups. It could potentially provide various coordination modes to build LCPs under appropriate synthesis conditions.

With the above in mind, we chose the $H_4$dppd ligand with different lanthanide ions and constructed a series of novel 2D Ln coordination polymers under hydrothermal conditions, namely, {$[La(Hdppd)(H_2O)_2\cdot(H_2O)_2]_n$(**1**), $[Ln_2(Hdppd)_2(H_2O)_4\cdot(H_2O)_3]_n$ [Ln = Sm(**2**), Eu(**3**)] and $[Ln(Hdppd)(H_2O)_3\cdot H_2O]_n$ [Ln = Gd(**4**), Tb(**5**), Dy(**6**), Ho(**7**), Er(**8**)]}. The structures were characterized using single-crystal X-ray diffraction analysis, elemental analysis, infrared (IR) spectroscopy and thermogravimetric analysis (TGA). The luminescence properties of **2**, **3**, **5** and **6** have also been investigated in detail. Spectral features and luminescence lifetime behavior are linked to the structural characteristics of the respective coordination polymers. The magnetic properties of **2**-**8** were discussed; **6** exhibits frequency dependent out-of-phase signals and **8** exhibits ferromagnetic coupling.

## Experimental section

**Materials.** All chemicals used were of reagent grade and were used without further purification. All syntheses were carried out in 25 mL Teflon-lined autoclaves under autogenous pressure. The reaction vessels were filled to approximately 50% volume capacity. Water used in the synthesis was distilled before use

**Physical Measurements.** The elemental analyses (C, H, and N) were carried out with a Perkin-Elmer 240C elemental analyzer. FT-IR spectra were recorded on a Nicolet IR-470 spectrometer using KBr pellets. Powder X-ray diffraction (PXRD) patterns of the samples were recorded using an X-ray diffractometer (BRUKER D8 ADVANCE) with Cu Kα radiation. Thermogravimetric analysis (TGA) experiments were performed on a NETZSCH TG 209 instrument applying a heating rate of 10 °C $min^{-1}$. Luminescence spectra were recorded on a FS920 steady state fluorescence spectrometer (Edinburgh Instruments) equipped with a Hamamatsu R928P red-sensitive photomultiplier for the visible range and a germanium detector for the near infrared. Luminescence decay measurements were obtained with a pulsed nitrogen laser (excitation wavelength of 337 nm, pulse length of 800 ps, repetition rate of 1Hz) and a 1024-channel Intensified CCD (Andor Technology) attached to a 0.5 m monochromator. The magnetic properties were measured on a Quantum Design MPMS-XL7 and a PPMS-9 ACMS magnetometer. Diamagnetic correction was made with Pascal's constants for all the constituent atoms.

**Single Crystal X-ray Crystallographic Study.** The collection of single crystal crystallographic data was carried out on a Bruker SMART Apex CCD diffractometer using graphite-monochromated Mo Kα radiation (0.71073 Å) at 293 K in the ω-2θ scan mode. An empirical absorption correction was applied to the data using the *SADABS* program. [12] The structures were solved by direct methods and refined by full-matrix least-squares methods on $F^2$ using the SHELXTL crystallographic software package. [13] All non-H atoms were refined anisotropically. The H atoms were placed in calculated positions and refined using a riding mode. The crystallographic data, selected bond lengths and angles for **1-8** are listed in Table 1, Table 2 and Table S1 (See Supporting Information), respectively. Crystallographic data for the structural analysis have been deposited with the Cambridge Crystallographic Data Center, CCDC 979204 for **1**, 979207 for **2**, 979201 for **3**, 979202 for **4**, 979208 for **5**, 979198 for **6**, 979203 for **7** and 979199 for **8**.

**Table 1** Crystal Data and Structure Refinement for **1-8**.

| Compound reference | **1** | **2** | **3** | **4** | **5** | **6** | **7** | **8** |
|---|---|---|---|---|---|---|---|---|
| Formula | $C_{15}H_{14}LaNO_{12}$ | $C_{30}H_{26}Sm_2N_2O_{23}$ | $C_{30}H_{26}Eu_2N_2O_{23}$ | $C_{15}H_{14}GdNO_{12}$ | $C_{15}H_{14}TbNO_{12}$ | $C_{15}H_{14}DyNO_{12}$ | $C_{15}H_{14}HoNO_{12}$ | $C_{15}H_{14}ErNO_{12}$ |
| Fw (amu) | 539.18 | 1083.23 | 1086.45 | 557.52 | 559.19 | 562.77 | 565.20 | 567.53 |
| Temp(K) | 293(2) | 293(2) | 293(2) | 293(2) | 293(2) | 293(2) | 293(2) | 293(2) |
| Cryst system | Monoclinic | Triclinic | Triclinic | Monoclinic | Monoclinic | Monoclinic | Monoclinic | Monoclinic |
| Space group | $P2_1/c$ | $P$-1 | $P$-1 | $P2_1/c$ | $P2_1/c$ | $P2_1/c$ | $P2_1/c$ | $P2_1/c$ |
| $a$ (Å) | 16.616(3) | 6.963(14) | 6.920(14) | 14.467(3) | 14.448(3) | 14.496(3) | 14.476(3) | 14.580(3) |
| $b$ (Å) | 6.645(13) | 10.796(2) | 10.760(2) | 7.252(15) | 7.194(14) | 7.199(14) | 7.181(14) | 7.188(14) |
| $c$ (Å) | 18.857(8) | 12.320(3) | 12.246(2)) | 20.749(7) | 20.630(7) | 20.714(7) | 20.617(7) | 20.756(7) |
| $\beta$(°) | 119.80(2) | 87.50(3) | 87.57(3) | 126.16(2) | 126.15(2) | 126.33(2) | 126.13(2) | 126.16(2) |
| $V$ (Å)$^3$ | 1806.6(9) | 854.6(3) | 841.2(3) | 1757.5(8) | 1731.4(8) | 1741.5(8) | 1731.0(8) | 1756.2(8) |
| $Z$ | 4 | 1 | 1 | 4 | 4 | 4 | 4 | 4 |
| $\rho_{calc}$ (g $cm^{-3}$) | 1.982 | 2.105 | 2.145 | 2.107 | 2.145 | 2.146 | 2.169 | 2.146 |
| $\mu$/$mm^{-1}$ | 2.433 | 3.504 | 3.798 | 3.844 | 4.156 | 4.362 | 4.643 | 4.849 |
| $F$(000) | 1056 | 528 | 530 | 1084 | 1088 | 1092 | 1096 | 1100 |
| Reflns collected/unique | 17746/4157 | 6997/2992 | 6982/2952 | 17078 / 4007 | 14156/3976 | 16730/3966 | 17108/3955 | 16620/3993 |
| GOF | 1.054 | 1.109 | 1.038 | 1.037 | 1.052 | 1.076 | 1.072 | 1.000 |
| $R_1$[a] ($I>2\sigma(I)$) | 0.0270 | 0.0353 | 0.0513 | 0.0305 | 0.0507 | 0.0246 | 0.0308 | 0.0454 |
| w$R_2$[b] | 0.0652 | 0.0878 | 0.1218 | 0.0729 | 0.1263 | 0.0579 | 0.0657 | 0.1185 |

[a] $R_1=\Sigma||F_o|-|F_c||/\Sigma|F_o|$. [b] $wR_2=\{\Sigma[w(F_o^2-F_c^2)^2]/\Sigma[w(F_o^2)^2]\}^{1/2}$.

**Preparation of Complexes 1-8.** A mixture of $H_4$dppd (0.2 mmol, 66.2 mg), rare earth nitrates ($Ln(NO_3)_3{\cdot}6H_2O$) [Ln = La (0.3 mmol, 129.9 mg), Sm (0.3 mmol, 133.3 mg), Eu (0.3 mmol, 134.0 mg), Gd(0.3 mmol, 135.3 mg), Tb (0.3 mmol, 135.8 mg), Dy (0.3 mmol, 136.9 mg), Ho (0.3 mmol, 137.7 mg) or Er(0.3 mmol, 138.4 mg)] and $H_2O$ (10 mL) was placed in a Teflon-lined stainless steel vessel, heated to 170 °C for 72 hours, and then cooled to room temperature over 48 hours. Yellow prism-shaped crystals of **1-7** and yellowish pink prism-shaped crystal of **8** were filtered off, washed with distilled water and dried in air.

Elem. anal. Calcd. (%) for **1**: C 33.41; H 2.62; N 2.60. Found: C 33.53; H 2.61; N 2.71. **2**: C 33.26; H 2.42; N 2.59. Found: C 33.37; H 2.46; N 2.53. **3**: C 33.16; H 2.41; N 2.58. Found: C 33.23; H 2.44; N 2.60. **4**: C 32.31; H 2.53; N 2.51. Found: C 32.25; H 2.64; N 2.46. **5**: C 32.22; H 2.52; N 2.50. Found: C 32.28; H 2.54; N 2.44. **6**: C 32.01; H 2.51; N 2.49. Found: C 32.11; H 2.43; N 2.39. **7**: C 31.88; H 2.50; N 2.48. Found: C 31.78; H 2.44; N 2.40. **8**: C 31.74; H 2.49; N 2.47. Found: C 31.69; H 2.44; N 2.38.

**IR** spectrum (KBr, $cm^{-1}$) for **1**: 3448s, 1701vs, 1653w, 1608vs, 1553w, 1467w, 1420w, 1384s, 1347w, 1270w, 1243m, 1197w, 1163m, 1125m, 1012m, 934w, 910m, 878w, 850w, 834m, 808m, 774m, 702m, 682w, 657w, 539w; **2**: 3371s, 1698m, 1612s, 1557s, 1465m, 1384vs, 1305m, 1261m, 1194m, 1165m, 1127s, 1091w, 1014m, 911m, 883w, 858w, 831w, 809w, 775w, 706m, 658m, 531w; **3**: 3549w, 3774s, 1692s, 1643s, 1602s, 1556m, 1465m, 1421s, 1384s, 1355m, 1303m, 1279m, 1247m, 1194w, 1164w, 1114w, 1091w, 1014m, 926w, 910m, 859m, 832w, 809w, 792w, 774m, 706m, 680w, 659w, 627w, 572w, 542w, 512w; **4**: 3397s, 2924w, 1690s, 1644s, 1604s, 1551m, 1465w, 1423m, 1384vs, 1356w, 1303m, 1279m, 1246m, 1194w, 1163w, 1127w, 1114m, 1091m, 1013m, 925w, 909w, 859m, 832w, 809w, 793w, 774m, 706m, 680w, 627w, 573w, 543w; **5**: 3548w, 3394s, 2924w, 1693s, 1644s, 1605s, 1552w, 1466w, 1424m, 1384vs, 1357w, 1303m, 1280m, 1246m, 1195w, 1164w, 1127w, 1114w, 1091w, 1014m, 925w, 909w, 859m, 832w, 809w, 793w, 775m, 680m, 660w, 628w, 573w, 544w, 513w, 428m; **6**: 3548w, 3388s, 2929w, 1692s, 1644s, 1606s, 1552w, 1466m, 1425s, 1384vs, 1357w, 1303m, 1280m, 1246m, 1195w, 1164w, 1127w, 1114w, 1091m, 1014m, 925w, 909w, 875w, 859m, 832w, 809w, 793w, 775m, 743w, 706m, 680m,

660w, 628w, 574w, 545w, 512w, 484w, 428w; **7**: 3405s, 2924w, 1693m, 1608m, 1466w, 1425m, 1384vs, 1303m, 1280m, 1246m, 1195w, 1164w, 1114w, 1091w, 1014w, 925vw, 859w, 832w, 809w, 775m, 706w, 680w, 628w, 574w, 546w, 428w; **8**: 3414s, 2924w, 1693m, 1637m, 1608m, 1467w, 1425m, 1384vs, 1303m, 1280m, 1245m, 1196w, 1164w, 1127w, 1114w, 1091w, 1014w, 925vw, 859w, 832w, 809w, 775w, 707w, 680w, 629w, 574w, 547w, 428w.

Since complexes **1**-**8** displayed similar IR spectra, that of **1** was chosen as an example for a detailed description. The IR spectrum of **1** showed the characteristic bands of carboxylate groups at 1701, 1653 and 1608 $cm^{-1}$. The wide absorption peak at 3448 $cm^{-1}$ is characteristic of O-H groups in water molecules. The absorption peaks of aromatic rings appeared at 1608, 1553 and 1467 $cm^{-1}$.

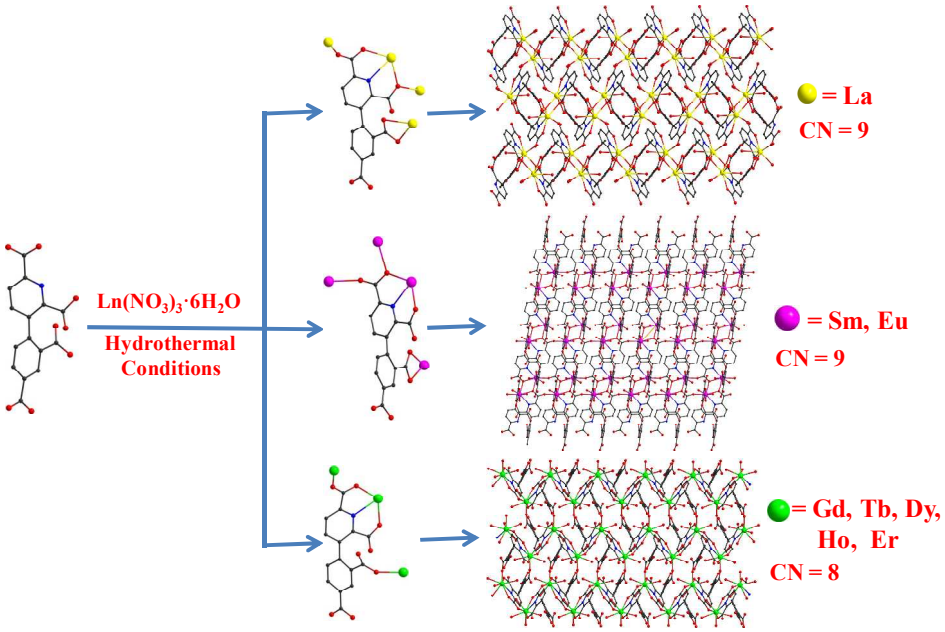


**Scheme 1** The synthetic route of **1**-**8**.

## Results and discussion

**Structure Description.** Because **2**-**3** and **4**-**8** are isomorphous, complexes **1**, **3**, and **7** were selected as representative examples to describe the crystal structures.

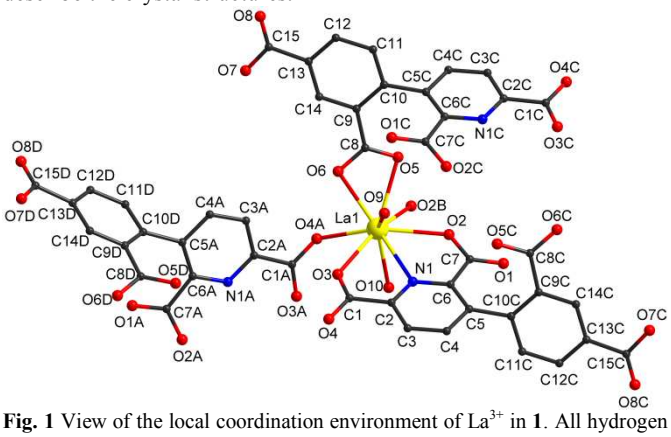


**Fig. 1** View of the local coordination environment of $La^{3+}$ in **1**. All hydrogen atoms and free lattice water molecules are omitted for clarity. Symmetry codes: (A) -x, -0.5+y, 1.5-z; (B) -x, 1-y, 2-z; (C) x, 2-y, 2-z; (D) x, 1.5-y, -0.5+z

**$[La(Hdppd)(H_2O)_2 \cdot (H_2O)_2]_n$ (1)**. X-ray crystal structure analyses revealed that **1** crystallizes in the space group $P2_1/c$. As illustrated in Fig. 1, the unit cell of **1** contains one $La^{3+}$, one Hdppd ligand, two coordinated water and two lattice water molecules. The coordination polyhedron around each $La^{3+}$ cation is nine coordinated in a slightly distorted tricapped trigonal prism geometry (Fig.S1A) with two sites occupied by oxygen atoms from two coordinated water molecules (O9, O10) and the remaining sites by O and N atoms from four Hdppd ligands (carboxyl O2B and O4A from two different ligands, O5 and O6 from carboxylic groups of the third ligand and O2, O3 and N1 from the fourth ligand). The La-O distances range from 2.4742(2) to 2.666(2) Å and the La-N distance is 2.293(2) Å, similar to the averages reported for La-O and La-N distances.

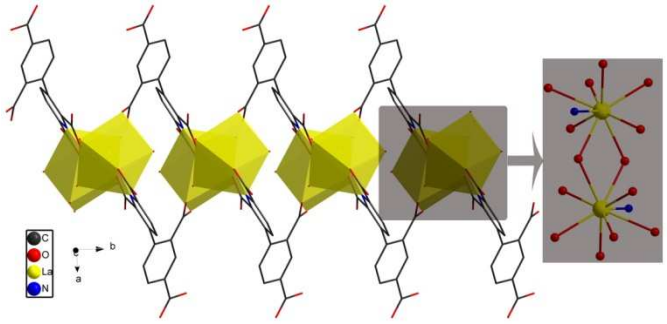

**Fig. 2** 1D chain along the *b* axis in **1**.

Each Hdppd ligand exhibits the same coordination mode in complex **1**: $(\kappa_1\text{-}\kappa_1\text{-}\mu_2)\text{-}\kappa_1\text{-}\kappa_2\text{-}(\kappa_1\text{-}\kappa_1\text{-}\mu_1)\text{-}\mu_4$ (Scheme 1), which links four $La^{3+}$ ions. The carboxyl O2 employs a $\mu_2$-O bidentate coordination mode to bridge two $La^{3+}$, resulting in a binuclear $La^{3+}$ center with the La-La distance of 4.0008(14) Å. The binuclear $La^{3+}$ centers are connected alternatively by carboxyl oxygen atoms (O5, O6) of Hdppd ligands to form a 1D linear chain along the *b* axis (Fig. 2). The infinite 1D chains extend to a 2D layer in the *bc* plane as a result of the coordinating carboxyl oxygen atoms (O4) from the Hdppd ligands with the $La^{3+}$ centers between the neighboring 1D chains along *c* axis (Scheme 1). Moreover, the 2D layers are

assembled into a 3D framework via hydrogen bonding interaction from the free water molecules and coordinated water molecules (O10–H10B···O11), and from the coordinating carboxylate oxygen atoms and the free water molecules (O7–H7···O12, O11–H11B···O8, O12–H12B···O1, O12–H12A···O4), as shown in Fig. S2.

**$[Ln_2(Hdppd)_2(H_2O)_4\cdot(H_2O)_3]_n$ [Ln = Sm(2), Eu(3)]**. From the single crystal X-ray diffraction study, it was found that complexes **2** and **3** are isostructural and crystallize in the space group *P*-1. Therefore the presentation and discussion will be restricted to complex **3** as a representative example. One $Eu^{3+}$ cation, one Hdppd ligand, two coordinated water and one and a half lattice water molecules are present in the asymmetric unit, as illustrated in Fig. 3. Similar to the complex **1**, each $Eu^{3+}$ ion is nine-coordinated in a $NO_8$ donor set with the coordination geometry of a slightly distorted tricapped trigonal prismatic configuration (Fig.S1B), formed by one nitrogen atom (N1) from the pyridine ring and two carboxyl oxygen atoms (O1, O3) of the same Hdppd ligand, two carboxyl oxygen atoms (O7C, O8C) from the second ligand, two carboxyl oxygen atoms (O1B, O2A) from the other two different ligands, and two oxygen atoms (O9, O10) from two coordinated water molecules. Therefore, there are four Hdppd ligands and two water molecules around the $Eu^{3+}$ ion. The Eu-O lengths range from 2.355(6) to 2.558(6) Å and the Eu-N length is 2.533(7) Å.

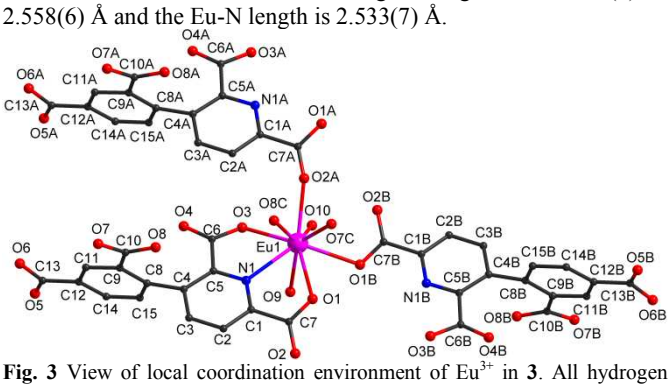


**Fig. 3** View of local coordination environment of $Eu^{3+}$ in **3**. All hydrogen atoms and free lattice water molecules are omitted for clarity. Symmetry codes: (A) 1+x, y, z; (B) 1-x, -1-y, 2-z; (C) 1-x, -y, 2-z

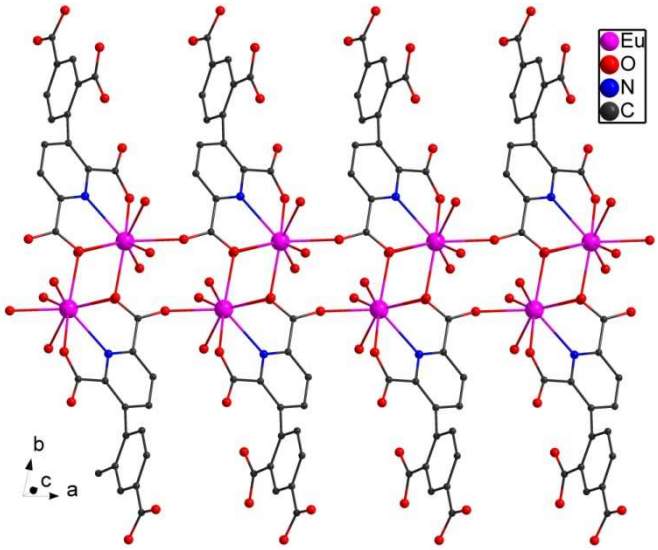


**Fig. 4** 1D chain along the *a* axis in **3**.

The coordination mode of the Hdppd ligand in complex **3** is ($\kappa_1$-$\kappa_2$-$\mu_3$)-$\kappa_1$-$\kappa_1$-($\kappa_1$-$\kappa_1$-$\mu_1$)-$\mu_4$ (Scheme 1), which is different from that of complex **1**. The carboxyl O1 of each Hdppd ligand adopts a $\mu_2$-O bidentate coordination mode bridging two $Eu^{3+}$ to build a similar binuclear center to complex **1**, with a Eu-Eu distance of 4.2619(16) Å. The binuclear $Eu^{3+}$ centers are linked by carboxyl O2 atoms to form a 1D chain along the *a* axis (Fig. 4). The further connection of binuclear $Eu^{3+}$ centers by carboxyl oxygen atoms (O7, O8) of the Hdppd ligands, extends the 1D chain to a 2D layer in the *ab* plane (Scheme 1). The 2D layers further assemble into a 3D framework via hydrogen bonding interactions (O6–H6···O4, O9–H9B···O11, O10–H10A···O5, O11–H11B···O6), as shown in Fig. S3, similar to the case observed in **1**.

**$[Ln(Hdppd)(H_2O)_3\cdot H_2O]_n$ [Ln = Gd(4), Tb(5), Dy(6), Ho(7), Er(8)]**. X-ray crystallography revealed that compounds **4-8** are isomorphous. Here, we choose **7** to represent the detailed structure. Complex **7** crystallizes in the space group $P2_1/c$. The structure of **7** is different from those of complexes **1** and **2-3.** First of all, the local coordination environment around the $Ho^{3+}$ ions is quite different. As indicated in Fig. 5, the unit cell of **7** contains one $Ho^{3+}$, one Hdppd ligand, three coordinated water molecules and one lattice water molecule. Each $Ho^{3+}$ is eight-coordinated with one nitrogen atom (N1A) and two carboxyl oxygen atoms (O2A, O3A) from the same Hdppd ligand, two carboxyl oxygen atoms (O1, O5B) from the other different ligands and three oxygen atoms (O9, O10, O11) from the coordinated water molecules. The coordination geometry is a distorted bi-capped triangular prism geometric configuration (Fig.S1C). The Ho-O and Ho-N distances are within normal ranges.

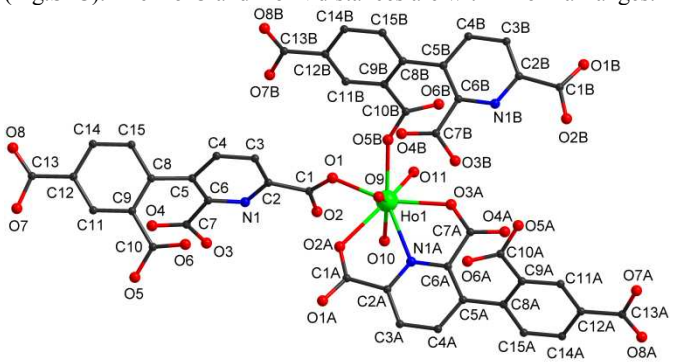


**Fig. 5** View of local coordination environment of $Ho^{3+}$ atom in **7**. All hydrogen atoms and free lattice water molecules are omitted for clarity. Symmetry codes: (A) 1-x, 0.5+y, 0.5-z; (B) x, 0.5-y, 0.5+z

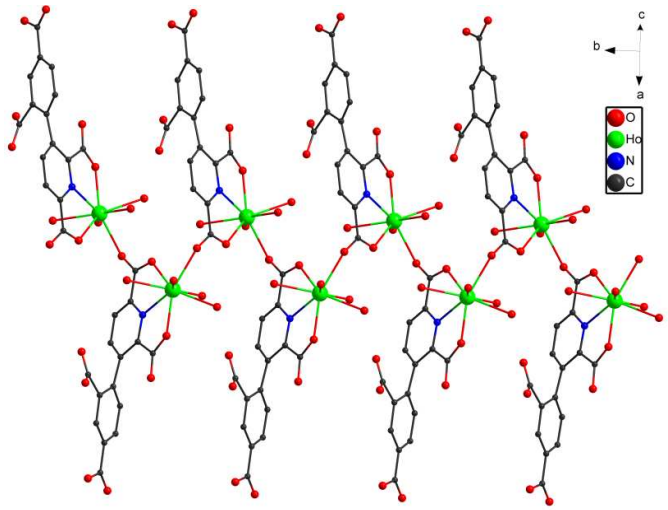


**Fig. 6** 1D chain along the *b* axis in **7**.

In addition, there are no binuclear $Ln^{3+}$ centers in **7** as found in complexes **1** and **2-3**. All Hdppd ligands have the same coordination

mode in **7:** ($\kappa_1$-$\kappa_1$-$\mu_2$)-$\kappa_1$-$\kappa_1$-$\kappa_1$-$\mu_3$ (Scheme 1). The 2-$COO^-$ of each Hdppd ligand adopt $\mu_1$- $\eta^1$: $\eta^1$ coordination modes to link the mononuclear $Ho^{3+}$ alternatively to a 1D infinite zigzag chain along the *b* axis (Fig. 6). The 2D layers and the 3D framework are assembled because of further connection of 1D chains and hydrogen bonding (O7–H7A···O12, O10–H10B···O8, O12–H12A···O1, O12–H12B···O4) between the 2D layers, similar to the cases in complexes **1** and **3** (Scheme 1, Fig. S4).

As shown in Scheme 1, complexes **1-8** were synthesized from the same ligand and in the similar reaction conditions, but three different crystal structures are obtained, which highlights some important aspects of the construction of lanthanide complexes. Although the lanthanide ions are all trivalent in these compounds, they adopt different coordination modes. Compounds **1-8** crystallize in three structural types with the coordination number of the Ln ions steadily decreasing from nine (**1** and **2-3**) to eight (**4-8**) as a result of the lanthanide contraction effect. Moreover, the average Ln-O bond lengths among **1-8** have also been compared. The average lengths between lanthanide and O atoms are decreasing continuously from 2.574(**1**), 2.498(**2**), 2.478(**3**), 2.400(**4**), 2.374(**5**), 2.372(**6**), 2.357(**7**) to 2.361(**8**) Å by an almost linear trend. Only in the complex **8**, the Er-O bond length slightly deviates from the average decline. In this series of complexes, the reason why the Hdppd ligand follows three different coordination models is presumably related to the change of the lanthanide ions' radius.

**PXRD and TGA.** Powder X-ray diffraction (PXRD) analyses of compounds **1-8** have been performed at room temperature (See Fig. S5 in Supporting Information). The patterns for **1-8** are in good agreement with the calculated patterns obtained from the single-crystal structures, confirming that the obtained purities equal those of the single crystal samples.

TGA curves for polycrystalline samples of **1-8** are depicted in Fig. S6 (see Supporting Information), and were carried out in the temperature range of 25-1000°C under $N_2$ ambient at a heating rate of 10 °C $min^{-1}$. Because the TGA curves of the eight complexes are very similar, only complex **1** was selected to examine the thermal stability. For **1**, the first weight loss of 13.26% in the range of 45-200 °C corresponds to the loss of four water molecules (calcd 13.35%, including two coordinated and two lattice water molecules). The second weight loss above 400 °C corresponds to the decomposition of the organic ligands. The residual weight of 30.83% (calcd: 30.20%) corresponds to $La_2O_3$.

**Luminescence.** As the 4f orbitals of the lanthanide ions are strongly embedded in the electronic configuration of the ion, the crystal structure has only minor influence on the position of the energy levels. As a consequence, the $4f^n$-$4f^n$ transitions give rise to rather narrow emission bands and high quantum efficiencies can be reached in for instance $Eu^{3+}$ and $Tb^{3+}$ doped materials, where multiphonon relaxation is often limited due to the relatively widely spaced energy levels. However, due to the high O-H phonon frequencies, hydrated crystals are generally known as less efficient luminescent materials, due to vibrational quenching. [14]

For **1** no relation between the luminescence and structural properties is possible as $La^{3+}$ is not luminescent because of the absence of 4f electrons. The $Gd^{3+}$ ion (complex **4**) can only emit in the UV range due to the large energy gap between the first excited state and the ground state. Finally, **7** and **8** do not show lanthanide based luminescence in the visible part of the spectrum. Both ions possess a large variety of energy levels, increasing the possibility of energy transfer to quenching centers, cross-relaxation and multiphonon relaxation resulting in low quantum efficiency for the transitions in the visible part of the spectrum. [15] Here, the luminescent properties of **2**, **3**, **5** and **6** were investigated in detail.

The excitation and emission spectra of **2**, **3**, **5** and **6** are shown in Fig. 7. As stated above, the emission spectra consist of intraconfigurational $4f^n$-$4f^n$ transitions. For $Sm^{3+}$, red luminescence is observed at 610 nm ($^4G_{5/2} - {}^6H_{7/2}$) and 650 nm ($^4G_{5/2} - {}^6H_{9/2}$). The spectrum of **3** is dominated by the hypersensitive $^5D_0$ - $^7F_2$ transition as a result of the absence of an inversion center in the site symmetry of $Eu^{3+}$. Due to this low site symmetry, the degeneracy of the Stark levels is almost completely lifted. For example, three emission peaks can be distinguished for the $^5D_0 - {}^7F_1$ transition at 585 nm, which is the maximum possible as each $^{2S+1}L_J$ multiplet term can split into at most 2J+1 crystal field levels. [16] The typical green emission is observed for the $Tb^{3+}$ compound **5**, dominated by the $^5D_4$ - $^7F_5$ transition (545 nm), together with additional peaks at 488 nm ($^5D_4$-$^7F_6$), 585 nm ($^5D_4$-$^7F_4$) and 620 nm ($^5D_4$ - $^7F_3$). The emission peaks of $Dy^{3+}$ (compound **6**) are situated in the 470 nm to 500 nm region ($^4F_{9/2} - {}^6H_{15/2}$) and the 550 nm to 600 nm region ($^4F_{9/2} - {}^6H_{13/2}$) resulting in a more or less white emission color.

The excitation spectrum consists of two broad bands in the 250 nm to 350 nm region, most probably due to ligand-to-metal transfer, next to the narrow $4f^n$-$4f^n$ transitions in the longer wavelength region (350 nm to 400 nm). Only for **6**, the energy transfer from the ligands to $Dy^{3+}$ is almost absent, as the excitation spectrum is dominated by the $4f^n$-$4f^n$ transitions.

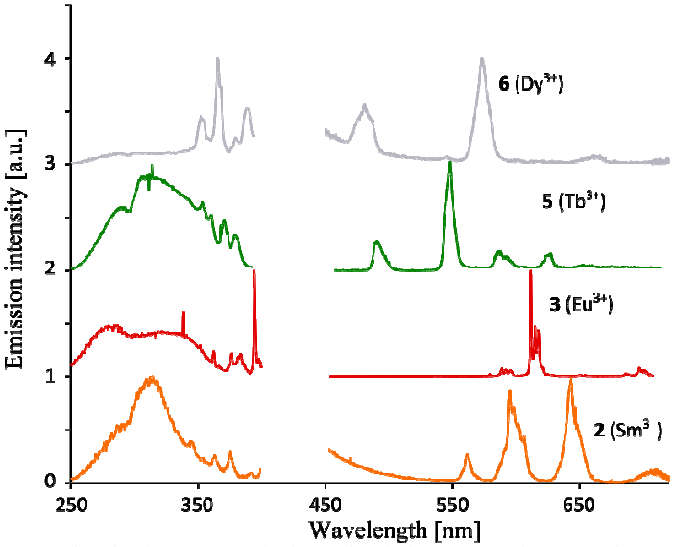


**Fig. 7** Photoluminescence excitation and emission spectra of compounds **2**, **3**, **5** and **6**. The excitation spectra monitored the emission at 643 nm (**2**), 611 nm (**3**), 545 nm (**5**) and 574 nm (**6**), respectively. The emission spectra were recorded upon excitation at 300 nm.

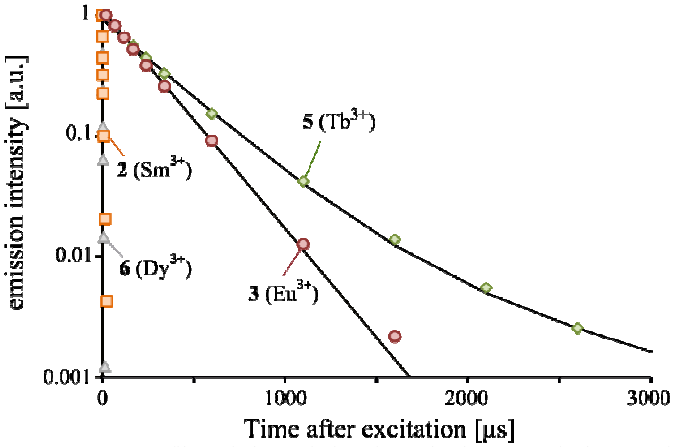


**Fig. 8** Decay profiles of the emission from the lowest excited state of compounds **2** (643 nm), **3** (611nm), **5** (545 nm) and **6** (574 nm) upon

excitation at 337 nm. The black lines are fits to the experimental data. Fitting values are given in the text.

In Fig. 8, the decay profiles for the emission starting from the lowest excited state of all studied compounds are shown. The observed decay rate results from the radiative decay rate and the non-radiative relaxation rates, including multiphonon quenching and cross-relaxation processes. Here, the high phonon frequencies of the hydrated compounds lead to prominent non-radiative decay paths, which yields a rather short observed decay constant and thus a low intrinsic efficiency for all compounds. A higher number of water molecules in the crystal increases this detrimental effect on the lifetime, especially in the case of water molecules coordinating the lanthanide ions. The emission intensity at any time after excitation can be described by $I(t) = I_0 \exp(-t/\tau)$, with $\tau$ the decay constant. A monoexponential fit resulted for all but one compounds in a good comparison between data and fit. For the decay of the $Tb^{3+}$ emission a bi-exponential function was needed to fit the data. The decay constants are $\tau = 3.0\mu s$ for $Sm^{3+}$, $\tau = 1.47$ µs for $Dy^{3+}$, $\tau_1 = 1073$ µs (10%) and $\tau_2 = 326$ µs (90%) for $Tb^{3+}$ and $\tau = 220$ µs for $Eu^{3+}$. Given that the radiative decay constants for $Eu^{3+}$ are typically in the millisecond range, the quenching influence of the water molecules in the first coordination sphere is strongly pronounced. [17]

The decay profile of the $^5D_0$ emission in **3** was investigated in more detail. Apparently, immediately after excitation, the $^5D_0$ level is additionally fed by another mechanism. This becomes clear in Fig. 9 where a rising component appears in the initial part of the decay curve. The most probable feeding mechanism is population from the higher lying $^5D_1$ level, with a difference between the $^5D_0$ and $^5D_1$ level of 1750 $cm^{-1}$. As the time scale of this feeding is two orders of magnitude smaller than the subsequent decay, an extra component can be added to the fit of the decay profile: $I(t) = I.\exp(-t/\tau) - I_{rise} \exp(-t/\tau_{rise})$, where the first component refers to the emptying and the last component to the filling of the $^5D_0$ level. We found a $\tau_{rise}$ (1.1µs) that matches quite well with the decay profile of the $^5D_1$ emission (Fig. 9), confirming the hypothesis of the relaxation of the majority of the $^5D_1$ population to the $^5D_0$ level.

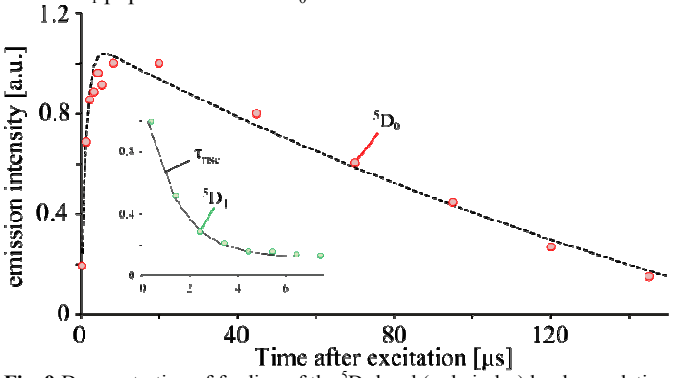


**Fig. 9** Demonstration of feeding of the $^5D_0$ level (red circles) by depopulation of the $^5D_1$ level (green circles, inset) in **3**. The dashed line is a fit of the form $I(t) = I.\exp(-t/\tau) - I_{rise}.\exp(-t/\tau_{rise})$.

**Magnetic Properties.** The direct current magnetic susceptibilities of **2-8** were measured under an applied magnetic field of 1000 Oe in the temperature range of 2 - 300 K. The plots of $\chi_m T$ vs. $T$ are presented in the Fig. 10 and 11. For **2**, The experimental plot of $\chi_m T$ vs. $T$ is nearly linear over the whole temperature range, which is similar to the reported behavior of $Sm^{3+}$ complexes. The $\chi_m T$ value gradually decreases from 0.793 $cm^3$ K $mol^{-1}$ at 300 K to 0.132 $cm^3$ K $mol^{-1}$ at 2 K. Because the $^6H$ ground state of $Sm^{3+}$ is split by spin-orbit coupling into six levels and the spin-orbit coupling parameter is of the order of 200 $cm^{-1}$, the first excited state $^6H_{7/2}$ can be populated at room temperature and above. [18] Therefore, both the crystal-field effect and the possible thermal population of the higher states for **2** should be considered. [19] At 2K, the $\chi_m T$ value of 0.132 $cm^3$ K $mol^{-1}$ is smaller than the value of 0.180 $cm^3$ K $mol^{-1}$ predicted by theory for two $Sm^{3+}$ ions, indicating the ground state $^6H_{5/2}$ of $Sm^{3+}$ ion is split into three Kramers doublets and/or very weak antiferromagnetic coupling is present between binuclear $Sm^{3+}$. Considering the existence of a strong spin-orbit coupling for $Sm^{3+}$ atoms and very weak antiferromagnetic coupling, the magnetic data can be analyzed using the free ion approximation. The molar magnetic susceptibility for **2** was fit by using the Eq. 1 (in Supporting Information) given by Andruh [18b] to obtain the spin-orbit coupling parameter. The fitting curve is drawn in Fig.10. The best fit to the magnetic susceptibilities of **2** in the whole temperature range gave the parameters $\lambda = 303$ $cm^{-1}$, with agreement factor defined as $R = \sum[(\chi_m)_{obs} - (\chi_m)_{calc}]^2/\sum[(\chi_m)_{obs}]^2) = 1.2 \times 10^{-5}$. The obtained parameters imply strong spin-orbit coupling, which is slightly lower than that given by Wang [19a] and higher than that reported by Andruh. [18b]

For **3**, the $\chi_m T$ is 2.55 $cm^3$ K $mol^{-1}$ at room temperature, which is much higher than the theoretical value of 0 $cm^3$ K $mol^{-1}$ for two uncoupled $Eu^{3+}$ ions ($S = 3$, $^7F_0$), but close to reported values. [20,18b] The high value of $\chi_m T$ mainly originates from the population of the first ($^7F_1$ for $Eu^{3+}$) and/or even higher excited states. Upon cooling, $\chi_m T$ rapidly reduces to 0.05 $cm^3$ K $mol^{-1}$ at 2 K, which can be explained as thermal depopulation of the excited levels. We tried to fit the $\chi_m T$ vs.$T$ curve to obtain the spin-orbit coupling parameter of **3** using the equation in literature, [20,18b] but this was not successful.

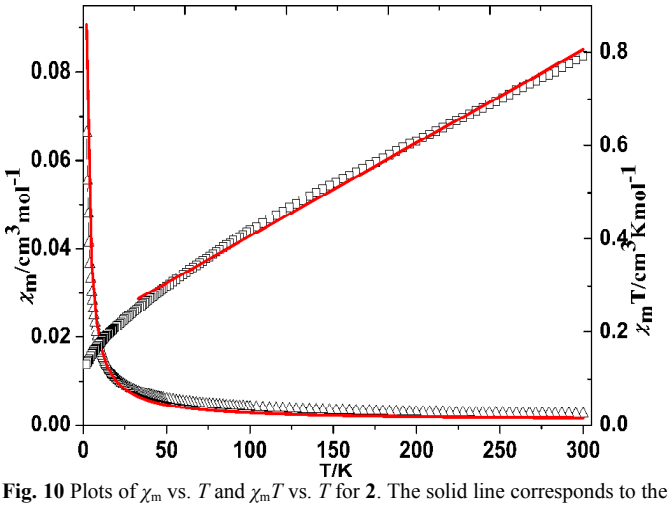


**Fig. 10** Plots of $\chi_m$ vs. $T$ and $\chi_m T$ vs. $T$ for **2**. The solid line corresponds to the best fit from 300 to 2 K.

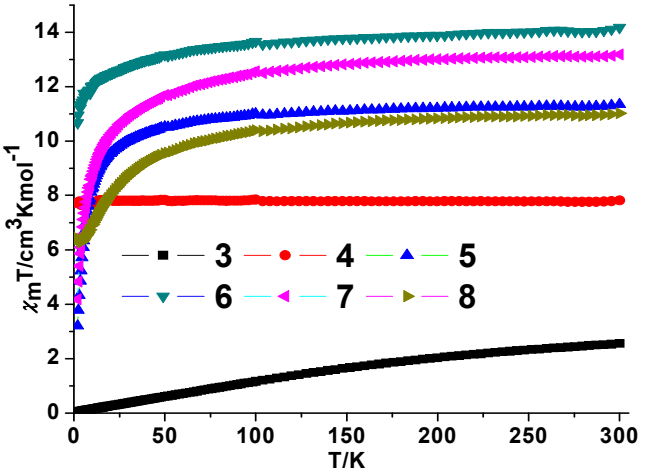

**Fig.11** Plots of $\chi_m T$ vs. $T$ for **3-8**.

For **4-8**, at 300 K, $\chi_m T$ values of 7.81, 11.35, 14.17, 13.18 and 11.02 $cm^3$ K $mol^{-1}$ were found, close to the expected values for one isolated $Gd^{3+}$ ($^8S_{7/2}$, $g$ = 2, $\chi_m T$ = 7.78 $cm^3$ K $mol^{-1}$), $Tb^{3+}$ ($^7F_6$, g = 3/2, $\chi_m T$ = 11.82 $cm^3$ K $mol^{-1}$), $Dy^{3+}$ ($^6H_{15/2}$, $g$ = 4/3, $\chi_m T$ = 14.17 $cm^3$ K $mol^{-1}$) , $Ho^{3+}$ ($^5I_8$, $g$ = 5/4, $\chi_m T$ = 14.07 $cm^3$ K $mol^{-1}$) and $Er^{3+}$ ($^4I_{15/2}$, $g$ = 6/5, $\chi_m T$ = 11.48 $cm^3$ K $mol^{-1}$) respectively. For **4**, with decreasing the temperature, the $\chi_m T$ value slowly decreases to the minimal value of 7.70 $cm^3$ K $mol^{-1}$. The $\chi_m^{-1}$ vs $T$ curve obeys the Curie-Weiss law (Fig. S7 in Supporting Information), fitting yields $C$ = 7.79 $cm^3$ K $mol^{-1}$ and $\theta$ = −1.19 K. The trend of the $\chi_m T$ vs. $T$ curve and the negative $\theta$ value prove the existence of antiferromagnetic interaction in **4**. For **5-7**, upon cooling, the $\chi_m T$ value slowly decreases to the minimal value of 3.20, 10.67 and 4.18 $cm^3$ K $mol^{-1}$, respectively. Since the depopulation of Stark sublevels can result in the decrease of $\chi_m T$ values with decreasing temperature, plots of $\chi_m T$ vs. $T$ cannot prove the presence of antiferromagnetic/ferromagnetic interactions in **5-7** [20]. For **8**, the $\chi_m T$ value slowly reduces to 6.27 $cm^3$ K $mol^{-1}$ at about 4 K, and then bounces to 6.42 $cm^3$ K $mol^{-1}$ at a temperature of 2 K (Fig. S8 in Supporting Information). This type of $\chi_m T$ vs. $T$ curve indicates the existence of ferromagnetic interactions in **8**. In the higher temperature region, the drop of $\chi_m T$ values caused by the depopulation of the Stark sublevels of $Er^{3+}$ may counteract the ferromagnetic coupling, and the ferromagnetic coupling is prominent below 4 K.

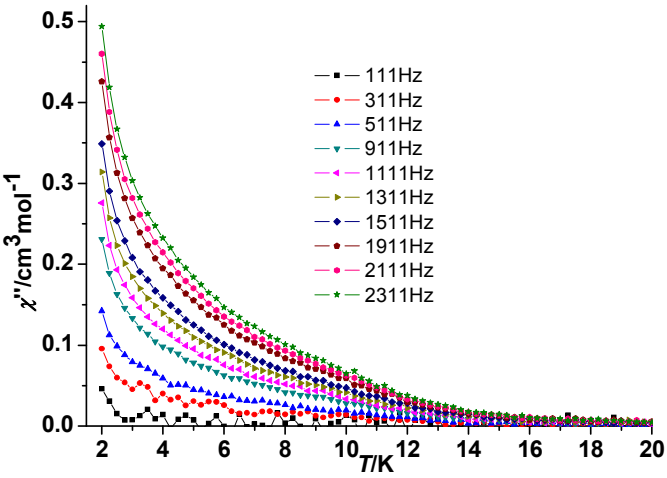


**Fig. 12** Temperature dependence of out of phase (χ") ac susceptibility components at different frequencies for **6** under zero dc field.

The field dependence of the magnetization ($M$) for **6** was measured at 2 K in the range of 0 - 8 T (Fig. S9 in Supporting Information). $M$ values rapidly increase when the magnetic field is below 10000 Oe, and then increase slowly to reach a maximum value of 5.62 $N\beta$ at 2 K in a field of 8 T, which is far lower than the expected saturation value of 10 $N\beta$. The unsaturated magnetization at 8 T may originate from strong magnetic anisotropy and/or low-lying excited states of $Dy^{3+}$ in **6**. [20a] Temperature dependencies of the alternating-current (ac) magnetic susceptibility for **6** were tested at zero direct-current (dc) field with an oscillation of 3 Oe between 111 - 2311Hz, and plots of χ" and χ' vs $T$ are depicted in Fig. S10 (in Supporting Information) and Fig. 12, respectively. Frequency dependent out-of-phase signals are clearly observed, indicating the onset of slow magnetization relaxation below about 10 K. However, peak values of χ" for **6** were not observed even up to 2311 Hz under zero dc field due to fast quantum tunneling of the magnetization. [21]

## Conclusions

In summary, eight new two-dimensional lanthanide coordination polymers based on the *N*-heterocyclic arylpolycarboxylate ligand, 3-(2, 4-dicarboxyphenyl)-2,6-pyridinedicarboxylic acid, were prepared and characterized. The LCPs show three different crystal structures and the Hdppd ligand follows three different coordination models, related to the lanthanide contraction effect. The luminescence properties of **2, 3, 5** and **6** were studied in detail. The compounds **3** and **5** show the typical bright red and green luminescence due to the $4f^n$-$4f^n$ transitions in $Eu^{3+}$ and $Tb^{3+}$, respectively, although the luminescence lifetime is shortened by non-radiative decay due to the presence of coordinating water molecules. The magnetic properties of **2-8** were measured and discussed. Compound **6** exhibits frequency dependent out-of-phase signals and **8** shows ferromagnetic coupling.

### Acknowledgements

This work was conducted in the framework of a project sponsored by the Natural Science Foundation of China (No.21071100), the Doctor Scientific Startup Foundation of Liaoning Province (No. 20111046) and the Distinguished Professor Project of Liaoning province. Katrien Meert is grateful to the Fund for Scientific Research (Flanders) for financial support.

### Notes and references

[a] *Laboratory of Coordination Chemistry, Shenyang University of Chemical Technology, Shenyang 110142, People's Republic of China. E-mail: sunyaguang@yahoo.com*

[b] *LumiLab, Department of Solid State Sciences, Ghent University, Ghent, Belgium.*

[c] *School of Materials and Metallurgy, Northeastern University, Shenyang 110004, People's Republic of China.*

† Electronic Supplementary Information (ESI) available: Represention of the TGA and PXRD diagrams of complexes **1-8**, and the selected bond lengths and bond angles of complexes **1-8**. See DOI: 10.1039/b000000x/

1 (*a*) Y. M. Yang, Q. Zhao, W. Feng and F. Y. Li, *Chem. Rev.*, 2013, **113**, 192; (*b*) J. Rocha, L. D. Carlos, F. A. A. Paz and D. Ananias, *Chem. Soc. Rev.*, 2011, 40, 926; (*c*) Y. J. Cui, Y. F. Yue, G. D. Qian and B. L. Chen, *Chem. Rev.*, 2011, **112**, 1126; (*d*) S. K. Mandal and H. W. Roesky, *Acc. Chem. Res.*, 2010, **43**, 248; (*e*) V. Chandrasekhar and B. Murugesapandian, *Acc. Chem. Res.*, 2009, **42**, 1047; (*f*) M. D. Allendorf, C. A. Bauer, R. K. Bhakta and R. J. T. Houk, *Chem. Soc. Rev.*, 2009, **38**, 1330.

2 (*a*) H. R. Moon, D. W. Lim and M. P. Suh, *Chem. Soc. Rev.*, 2013, **42**, 1807; (*b*) M. Yoon, R. Srirambalaji and K. Kim, *Chem.Rev.*, 2012, **112**, 1196 (*c*) J. Lee, O. K. Farha, J. Roberts, K. A. Scheidt, S. T. Nguyen and J. T. Hupp, *Chem. Soc. Rev.*, 2009, **38**, 1450; (*d*) L. Ma, C. Abney and W. Lin, *Chem. Soc. Rev.*, 2009, **38**,1248.

3 (*a*) X. J. Feng, W. Z. Zhou, Y. G. Li, H. S. Ke, J. K. Tang, R. Clérac, Y. H. Wang, Z. M. Su and E. B. Wang, *Inorg. Chem.*, 2012, **51**, 2722; (*b*) L. Sorace, C. Benelli and D. Gatteschi, *Chem. Soc. Rev.*, 2011, **40**, 3092; (*c*) K. Biradha, C. Y. Su and J. J. Vittal, *Cryst. Growth Des.*, 2011, **11**, 875; (*d*) T. K. Prasad, M. V. Rajasekharan and J. P. Costes, *Angew. Chem. Int. Ed.*, 2007, **46**, 2851; (*e*) Y. F. Zhou, M. C. Hong and X. T. Wu, *Chem. Commun.*, 2006, **42**, 135.

4 (*a*) T. A. Makal, J. R. Li, W. Lu and H. C. Zhou, *Chem. Soc. Rev.*, 2012, **41**, 7761; (*b*) M. P. Suh, H. J. Park, T. K. Prasad and D. W. Lim, *Chem.Rev.*, 2012, **112**, 782; (*c*) P. Cui, Y. G. Ma, H. H. Li, B. Zhao, J. R. Li, P. Cheng, P. B. Balbuena, and H. C. Zhou, *J. Am. Chem. Soc.*, 2012, **134**, 18892; (*d*) M. Fang, B. Zhao, Y. Zuo, J. Chen, W. Shi, J. L. and P. Cheng, *Dalton Trans.*, 2009, **38**, 7765; (*e*) B. D. Chandler, J. O. Yu, D. T. Cramb and G. K. H. Shimizu, *Chem. Mater.*, 2007, **19**, 4467.

5 (*a*) P. Nugent, Y. Belmabkhout, S. D. Burd, A. J. Cairns, R. Luebke, K. Forrest, T. Pham, S. Ma, B. Space, L. Wojtas, M. Eddaoudi and M. J. Zaworotko, *Nature*, 2013, **495**, 80; (*b*) K. Sumida, D. L. Rogow, J. A. Mason, T. M. McDonald,E. D. Bloch, Z. R. Herm, T. H. Bae and J. R. Long, *Chem.Rev.*, 2012, **112**, 724; (*c*) H. Wu, Q. Gong, D. H. Olson and J. Li, *Chem. Rev.*, 2012, **112**, 836; (*d*) E. D. Bloch, W. L. Queen, R. Krishna, J. M. Zadrozny,C. M. Brown and J. R. Long, *Science*, 2012, **335**, 1606; (*e*) J. R. Li, J. Sculley and H. C. Zhou, *Chem. Rev.*, 2011, **112**, 869; (*f*) J. R. Li, R. J. Kuppler and H.-C. Zhou, *Chem. Soc. Rev.*, 2009, **38**, 1477.

6 (*a*) Y. Wang, Z.-J. Zhang, W. Shi, P. Cheng, D.-Z. Liao and S. P. Yan, *CrystEngComm*, 2010, **12**, 1086; (*b*) Y. P. Cai, Q.-Y. Yu, Z. Y. Zhou, Z. J. Hu, H. C. Fang, N. Wang, Q. G. Zhan, L. Chen and C. Y. Su, *CrystEngComm*, 2009, **11**, 1006; (*c*) X. Q. Zhao, B. Zhao, S. Wei and P. Cheng, *Inorg. Chem.*, 2009, **48**, 11048; (*d*) W. X. Chen, Y. P. Ren, L. S. Long, R. B. Huang and L. S. Zheng, *CrystEngComm*, 2009, **11**, 1522; (*e*) S. C. Xiang, S.-M. Hu, T. L. Sheng, L. Chen and X. T. Wu, *Struct. Bond.*, 2009, **133**, 161; (*f*) F. N. Shi, L. Cunha-Silva, R. A. Sa´ Ferreira, L. Mafra, T. Trindade, L. D. Carlos, F. A. Almeida Paz and J. Rocha, *J. Am. Chem. Soc.*, 2008, **130**, 150; (*g*) P. Wang, J. P. Ma, Y. B. Dong and R. Q. Huang, *J. Am. Chem. Soc.*, 2007, 129, 10620; (*h*) K. C. Szeto, K. P. Lillerud, M. Tilset, M. Bjørgen, C. Prestipino, A. Zecchina, C. Lamberti and S. Bordiga, *J. Phys. Chem. B*, 2006, **110**, 21509; (*i*) Y. Q. Sun, J. Zhang and G. Y. Yang, *Chem. Commun.*, 2006, **42**, 4700.

7 (*a*) P. F. Shi, B. Zhao, G. Xiong, Y. L. Hou and P. Cheng, *Chem. Commun.*, 2012, **48**, 823; (*b*) X. Q. Zhao, P. Cui, B. Zhao, W. Shi and P. Cheng, *Dalton Trans.*, 2011, **40**, 805; (*c*) B. Zhao, X. Q. Zhao, Z. Chen, W. Shi, P. Cheng, S. P. Yan and D. Z. Liao, *CrystEngComm*, 2008, **10**, 1144.

8 (*a*) J. C. G. Bünzli and C. Piguet, *Chem. Rev*. 2002, **102**, 1897; (*b*) B. Moulton and M. J. Zaworotko, *Chem. Rev*. 2001, **101**, 1629.

9 (*a*) X. Zhao, D. X. Wang, Q. Chen, J. B. Chen, G.-Y. Lin, S. T. Yue and Y. P. Cai, *Inorg. Chem. Commun.*, 2012, 23, 127; (*b*) S. C. Xiang, S. M. Hu, T. L. Sheng, J. S. Chen and X. T. Wu, *Chem. Eur. J.*, 2009, **15**, 12496; (*c*) Z. He, E. Q. Gao, Z. M. Wang, C. H. Yan and M. Kurmoo, *Inorg. Chem.*, 2005, **44**, 862; (*d*) L. Pan, X. Y. Huang, J. Li, Y. G. Wu and N. W Zheng, *Angew. Chem. Int. Ed.*, 2000, **39**, 527.

10 (*a*) S. J. Wang, Y. W. Tian, L. X. You, F. Ding, K. W. Meert, D. Poelman, P. F. Smet, B. Y. Ren and Y. G. Sun, *Dalton Trans.*, 2014, **43**, 3462; (*b*) X. H. Chang, J. H. Qin, L. F. Ma, J. G. Wang and L. Y. Wang, *Cryst. Growth Des.*, 2012, **12**, 4649; (*c*) D. Tian, Y. Pang, Y. H. Zhou, L. Guan and H. Zhang, *CrystEngComm*, 2011, **13**, 957; (*d*) I. A. Ibarra, S. H. Yang, X. Lin, A. J. Blake, P. J. Rizkallah, H. Nowell, D. R. Allan, N. R. Champness, P. Hubberstey and M. Schroder, *Chem. Commun.*, 2011, **47**, 8304; (*e*) S. T. Zheng, F. Zuo, T. Wu, B. Irfanoglu, C. Chou, R. A. Nieto, P. Y. Feng and X. H. Bu, *Angew. Chem., Int. Ed.*, 2011, 50, 1849; (*f*) A. G. Wong-Foy, O. Lebel and A. J. Matzger, *J. Am. Chem. Soc.*, 2007, **129**, 15740. (*g*) C. Serre, C. Mellot-Draznieks, S. Surblé, N. Audebrand, Y. Filinchuk and G. Férey, *Science*, 2007, **315**, 1828.

11 (*a*) X. Feng, Y. Q. Feng, L. Liu, L. Y. Wang, H. L. Song and S. W. Ng, *Dalton Trans.*, 2013, **42**, 7741; (*b*) X. Feng, X. L. Ling, L. Liu, H. L. Song, L. Y. Wang, S. W. Ng and B. Y. Su, *Dalton Trans.*, 2013, **42**, 10292; (*c*) X. Feng, L. F. Ma, L. Liu, L. Y. Wang, H. L. Song, and S. Y. Xie, *Cryst. Growth Des.*, 2013, **13**, 4469; (*d*) X. Feng, J. G. Wang, B. Liu, L. Y. Wang, J. S. Zhao, and S. W. Ng, *Cryst. Growth Des.*, 2012, **12**, 927; (*e*) S. J. Wang, Y. W. Tian, G. Xiong, L. X. You, F. Ding, M. Y. Guo, E. J. Gao, P. F. Smet, D. Poelman, L. J. Xiao and Y. G. Sun, *CrystEngComm*, 2012, **14**, 8689; (*f*) Y. G. Sun, G. Xiong, M. Y. Guo, F. Ding, S. J. Wang, P. F. Smet, D. Poelman, E. J. Gao and F. Verpoort, *Dalton Trans.*, 2012, 41, 7670; (*g*)Z. S. Bai, J. Xu, T. Okamura, M. S. Chen, W. Y. Sun and N. Ueyama, *Dalton Trans.*, 2009, 2528; (*h*) M. S. Liu, Q. Y. Yu, Y. P. Cai, C. Y. Su, X. M. Lin, X. X. Zhou, and J. W. Cai, *Cryst. Growth Des.*, 2008, **8**, 4083; (*i*) Y. Q. Sun, J. Zhang and G. Y. Yang, *Chem. Commun*., 2006, **42**, 4700; (*j*) C. Qin, X. L. Wang, E. B. Wang and L. Xu, *Inorg. Chem. Commun.*, 2005, **8**, 9; (*k*) X. L. Wang, C. Qin, E. B. Wang and L. Xu, *J. Mol. Struct.*, 2005, **749**, 45; (*l*) Y. Q. Sun, J. Zhang, Y. M. Chen and G. Y. Yang, *Angew. Chem. Int. Ed.*, 2005, **44**, 5814.

12 G. M. Sheldrick, *Program SADABS: Area-Detector Absorption Correction*, University of Göttingen: Germany, 1996.

13 (*a*) G. M. Sheldrick, *Acta Cryst.* 2008, A**64**, 112; (*b*) G. M. Sheldrick, *SHELXL-97*, University of Göttingen: Göttingen, Germany, 1997.

14 H. W. Moos, *J. Lumin*., 1970, **1-2**, 106.

15 W. M. Yen, S. Shionoya and H. Yamamoto, *Phosphor Handbook, 2nd Edition*, CRC Press, Boca Raton, 200**7**, pp. 192-211.

16 P. A. Tanner, *Chem. Soc. Rev.*, 2013, **42**, 5090.

17 F. N. Shi, D. Ananias, T. H. Yang and J. Rocha, *J. Solid State Chem*., 2013, **204**, 321.

18 (*a*) L. Zhao, S.-Y. Lin, S. Shen, and J.-K. Tang, *Inorg. Chem. Commun.*, 2011, **14** 1928; (*b*) M. Andruh, E. Bakalbassis, O. Kahn, J. C. Trombe and P. Porchers, *Inorg. Chem*., 1993, **32**, 1616.

19 (*a*) X. Feng, L. L. Zhou, L. Y. Wang, J. G. Zhou, Z. Q. Shi and J. J. Shang, *Inorg.Chim. Acta*, 2013, **394**, 696; (*b*)X. D.Yang, C. H. Zhang, D. P. Wang and Y. G. Chen' *Inorg. Chem. Commun*., 2010, **13**, 1350.

20 (*a*) Y. L. Hou, G. Xiong, B. Shen, B. Zhao, Z. Chen and J. Z. Cui' *Dalton Trans.*, 2013, **42**, 3587; (*b*) B. M. Ji, D. S. Deng, X. He, B. Liu, S. B. Miao, N. Ma, W. Z. Wang, L. G. Ji, P. Liu and X. F. Li, *Inorg. Chem.*, 2012, **51**, 2170.

21 (*a*) P. F. Shi, G. Xiong, B. Zhao, Z. Y. Zhang and P. Cheng, *Chem. Commun.*, 2013, **49**, 2338; (*b*) G. Xiong, X. Y. Qin, P. F. Shi, Y. L. Hou, J. Z. Cui and B. Zhao, *Chem. Commun.*, 2014, **50**, 4255.

## Graphical Abstract

# Synthesis, Structure and Properties of 2D Lanthanide Coordination Polymers Based on *N*-heterocyclic Arylpolycarboxylate Ligands

**Li-Xin You, Shu-Ju Wang, Gang Xiong, Fu Ding, Katrien W. Meert, Dirk Poelman, Philippe F. Smet, Bao-Yi Ren, Yan-Wen Tian, and Ya-Guang Sun***

Eight 2D LCPs based on the *N*-heterocyclic arylpolycarboxylate ligands were prepared, and the luminescence and magnetic properties were studied.